Cite this paper: Vietnam J. Chem., **2022**, *60(3)*, 307-316 Research article
DOI: 10.1002/vjch.202100116

Investigations into the electronic properties of lorlatinib, an anti-cancerous drug using DFT, wavefunction analysis and MD simulations

Jamelah S. Al-Otaibi[1], Y. Sheena Mary[2*], Y. Shyma Mary[2], M. Thirunavukkarasu[3,4]

[1]*Department of Chemistry, College of Science, Princess Nourah Bint Abdulrahman University, Saudi Arabia*

[2]*Thushara, Neethinagar-64, Pattathanam, Kollam, Kerala, India*

[3]*Department of Physics, Indo-American College, Cheyyar, Tamil Nadu, India*

[4]*Department of Physics, Thiru A Govindasamy Govt. Arts College, Tindivanam, Tamil Nadu, India*

Submitted August 29, 2021; Revised October 9&18, 2021; Accepted October 24, 2021

Abstract

Lung cancer is a kind of cancer with high morbidity and mortality rate, making it one of the most dangerous tumors to humanity's health and existence. Wavefunction dependent reactivity analysis, atom in molecule (AIM) and molecular dynamics (MD) simulations of lorlatinib (LTB) are reported in the present work. Electrophilicity index predicts the biological activity. The bond ellipticity describes the anisotropy of the curvature of electron density and its maximum value is at C15-H32. Chemical environments, N8=C26-N7, C18=C30≡N9, and C15=C14-C13 are found to be highest delocalization regions. The complexes were stable throughout the simulation and amino acids involved in bringing the overall structural deviation are explored.

Keywords. DFT, MD simulations, lorlatinib, anti-cancer activity, reactivity analysis.

1. INTRODUCTION

Lung cancer has a high death rate and is a dangerous tumor to mankind's health and existence.[1] Majority of people with lung adenocarcinomas are diagnosed with lung cancer.[2] Over the last few decades, scientific study has centered on figuring out how tumors form.[3] One of the most important causes causing cancer sickness, according to studies, is the accumulation of genetic and epigenetic alterations.[4] As a result, there is a lot of interest in developing highly sensitive and precise medications for cancer treatment. Chemotherapy has been the standard treatment for lung cancer for decades, despite its negative side effects.[5] However, tremendous progress is in the field of lung cancer treatment in recent years, notably with the advent of targeted medicines. The discovery of possible driver mutations in lung cancer gave rise to the concept of targeted therapy.[6] The success of ctrizotinib, FDA-approved Anaplastic lymphoma kinase (ALK) inhibitor, demonstrated efficacy of targeted therapy.[7,8] Despite the fact that these ALK inhibitors have revolutionized lung cancer treatment, tumors have been observed to relapse. Resistance mechanisms include changes in the therapeutic target, signaling system modification and severe toxicity profiles.[9] Therapeutic molecule discovery is a time consuming process since many elements of a compound's safely, pharmacokinetics and efficacy must be refined before it can be considered as a drug candidate. With the ability to design tiny drugs quickly and cheaply, computed aided approaches have significantly altered the situation. MD screening and pharmacophore modeling approaches, in particular, are being used effectively in pharmacology. MD methods, for example, were employed to investigate the mechanism of nalidixic acid resistance and to determine the reason of oseltamivir resistance.[10,11] Lorlatinib is a third generation, ATP-competitive small molecule tyrosine kinase inhibitor which shows success in clinical studies in lung cancer patients.[12] Lorlatinib is a macrocyclic molecule that has a new chemical structure that allows it to penetrate cells and block efflux.[13] Jiang et al. published a structural analysis of the cyclic anticancer drug lorlatinib.[14] The structural investigations, density functional theory (DFT) studies on selpercatinib and IR spectroscopy with DFT studies of erlotinib were reported.[15,16] Due to the anti-cancerous activity of lorlatinib (LTB), the reactivity analysis together with AIM and MD simulations are reported.

2. METHODS

The optimization of LTB[17,18] with B3LYP/6-311++G(d,p) (Fig.1) and same basis set is used for conformational analysis, frontier molecular orbitals (FMOs), molecular electrostatic potential (MEP) and natural bond orbital (NBO) calculations. Molecular geometry was fully optimized by Berny's optimization method and no imaginary wavenumbers were obtained proving that a true minimum on the potential surface. Electron localization function (ELF), Localized orbital locator (LOL), and AIM and Reduced density gradient (RDG) studies have been used to investigate the topological properties of LTB by using Multiwfn 3.6 program and AIMAll software.[19,20] It was found that this method provide significant information about the amounts of electron density and intramolecular characteristics of a system. The electron density, Laplacian of electron densities and ellipticity parameters at the bond critical points for LTB were tabulated from AIMAll calculations. Electron localization function using Multiwfn software was used to achive surface analysis in which ELF is measured by applying Pauli repulsion principle to two like-spin electrons, which can be used to study electron localization in the molecular system. RDG graph gives the closed-shell weak interactions between atoms in a molecule.

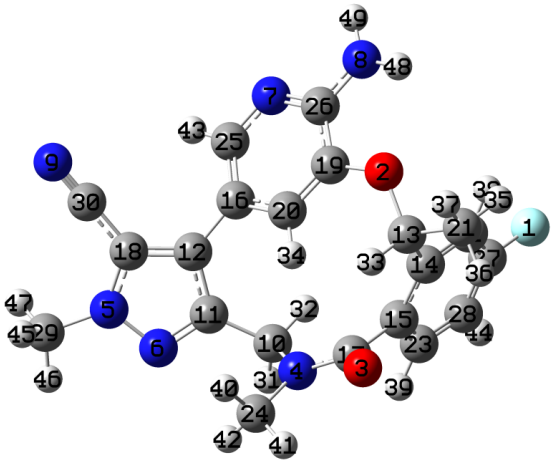

Figure 1: Optimized geometry of LTB

System builder from Desmond 2019 was used to create a system that included protein alone (APO) and protein-Ligand complex (DRG) with solvent for simulation purposes.[21] The OPLS force field was added to the system and SPC water system was utilized to mimic the solvent along with a cubic box. To neutralize the systems, 1.5 mM of NaCl ions are supplied to the water-filled box of size 35 nm^3. The Desmond program's MD tool was used for simulation time to 100 ns under normal NTP (constant number of particles N, pressure P and temperature T) settings with the model system relaxed before to the simulation. The simulation interactive diagram tool examined the simulation data in a graphical manner providing features of protein-ligand combination over the simulation period. To further corroborate docking findings, we looked at RMSD, RMSF, and H-bond interaction data.

3. RESULTS AND DISCUSSION

3.1. Chemical and electronic properties

The FMOs (figure 2) are undergone chemical reactions due to electron transfers from occupied to the unoccupied molecular orbitals. HOMO is delocalized over pyridine and N-N containing rings while LUMO is over pyridine and phenyl rings which are evident for the charge transfer within the system. The different chemical descriptors are (eV): EHOMO = -7.7780, ELUMO = -4.7377, energy gap = 3.0403, hardness = 1.5202, chemical potential =

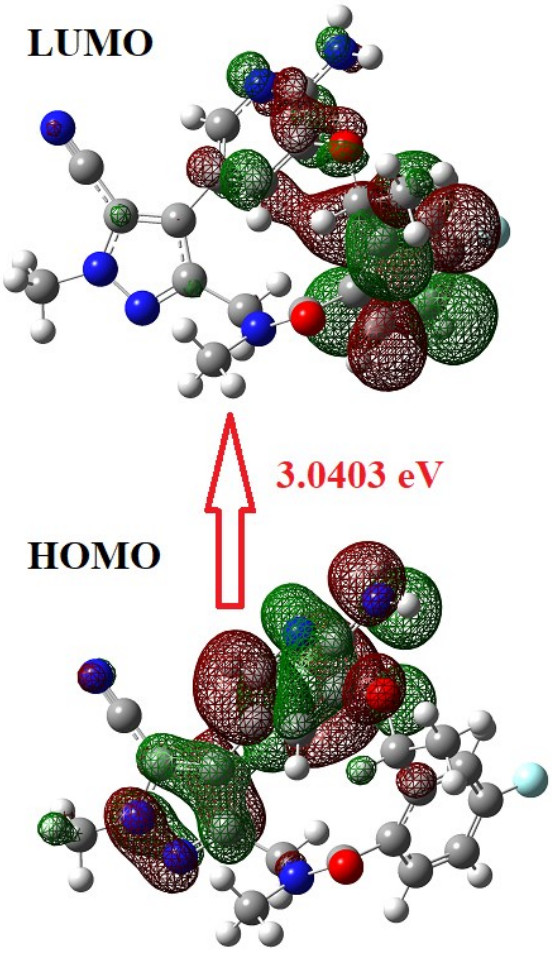

Figure 2: FMOs plot of LTB

-6.2579 and electrophilicity index = 12.8801.[22] The value of electronegativity and hardness are a measure of capacity of the molecule to attract electrons and the resistance of an atom to charge transfer. Electrophilicity index predicts the stabilization energy when its electrons are saturated and can even be used to predict biological activity. According to Jiang et al.[14] the global reactivity descriptors (a.u.) of lorlatinib are 0.21794 (ionization potential), 0.06768 (electron affinity), -0.14281 (chemical potential), 0.07513 (hardness) and 0.27146 (electrophilicity index).

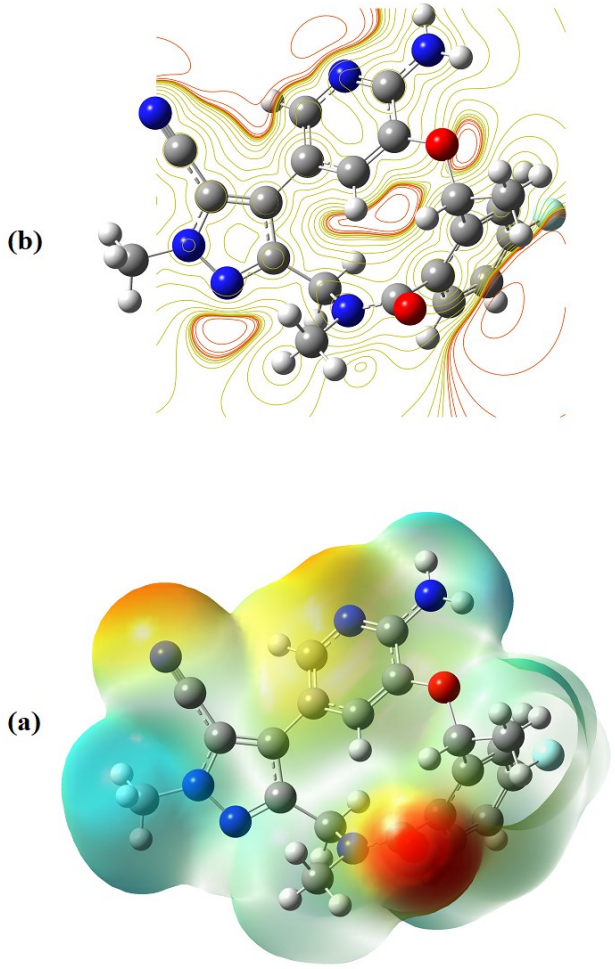

Figure 3: (a) MEP plot of LTB, (b) ESP contour plot of LTB

MEP is employed in biological recognition processes to predict target binding locations, electron donor and acceptor areas.[23] The sensitivity of electrostatic potential was depicted on MEP surface (figure 3) using different colours; red and blue colours signify high electronegative and electropositive potentials. The red and yellow patches were caused by oxygen atoms, nitrogen atom in C≡N and pyridine ring in LTB. Higher electronegative and electropositive patches were found over these atoms indicating nucleophilic and electrophilic attack sites, as seen on the contour map.[24]

Very strong NBO hyper conjugative interactions (energy in kcal/mol) are produced by lone pair atoms as[25]: F1→C22-C27 (19.74), O3→(N14-C17, C15-C17) (25.06, 19.38), N4→O3-C17 (47.17), N5→(N5-C11, C12-C18)(31.07, 39.04), N7→C19-C26 (12.31), N8→N7-C26 (52.63), N9→C18-C30 (12.79). The high delocalization energies indicate that the molecule is inherently stable due to hyper conjugative delocalization.

3.2. AIM analysis

The AIM analysis explains the bonding interactions in various chemical systems, which is based on topological features of electron density (ED). According to AIM study, any pair of atoms in a molecular system connected has a single critical point (BCP) and it was used to explain chemical bonding in molecular structure. In this present case, the ED $\rho(r)$, second derivative ED of Laplacian $\nabla^2\rho(r)$, kinetic ED $G(r)$, local energy density $H(r)$, potential ED $V(r)$, ellipticity (ε), and ratio of – (G/V) were calculated for selected BCPs and are seen in table 1. The AIM Molecular graph of the LTB was shown in figure 4, as we have seen in this figure bond paths (black lines), BCP's (green spheres), ring path (ash color solid lines), RCP's

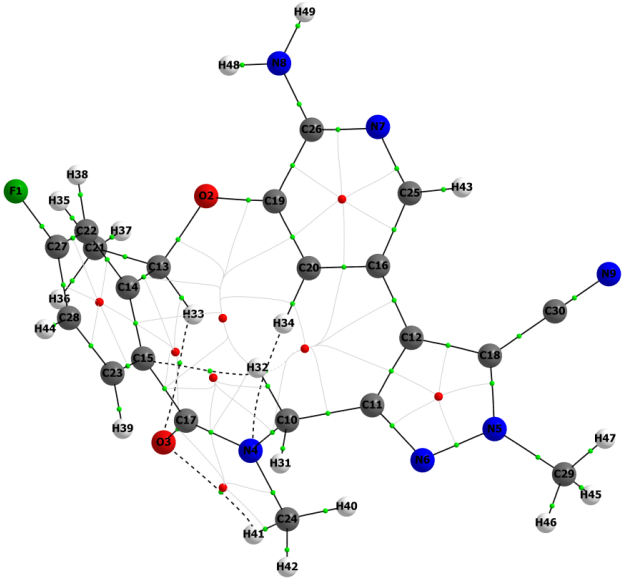

Figure 4: AIM Molecular graph of LTB: a green small spheres (BCPs), small red sphere (RCBs), black lines (bond paths), ash color solid lines (RCP to BCP ring path), block dotted lines (Non-covalent weak interactions)

(red sphere), Non-covalent weak interactions (black

dotted lines). The Laplacian electron density $\nabla^2\rho(r)$ and electron density $\rho(r)$ and were utilized to assess the atomic strength attributes and molecular interactions at BCPs. Generally, the value of $\rho(r) \geq 0.14$ & $\nabla^2\rho(r) < 0$ a.u., shows that the existence of shared interactions of covalent bond, whereas the $\rho(r) \leq 0.05$ & $\nabla^2\rho(r) > 0$ a.u., indicates that the closed-shell interactions.[26]

Table 1: Topological parameters of the selected BCPs for LTB

BCP	ρ(r) (a.u.)	∇^2ρ(r) (a.u.)	V(r) (a.u.)	G (r) (a.u.)	H(r) (a.u.)	-(G/V)	ε
C15 - H32	0.0159	0.0555	-0.0110	0.0125	0.0014	1.1283	1.7268
O3 - H41	0.0209	0.0909	-0.0199	0.0213	0.0014	1.0704	1.7101
N4 - H34	0.0140	0.0556	-0.0110	0.0124	0.0015	1.1337	1.0548
O3 - H33	0.0153	0.0656	-0.0123	0.0144	0.0020	1.1654	0.3696
C19 - C26	0.2838	-0.8230	-0.3879	0.0911	-0.2968	0.2348	0.1891
N6 - C11	0.3039	-0.5670	-0.5209	0.1896	-0.3313	0.3639	0.1727
C14 - C15	0.2888	-0.8283	-0.4113	0.1021	-0.3092	0.2483	0.1646
C14 - C22	0.2937	-0.8556	-0.4228	0.1045	-0.3184	0.2470	0.1601
C15 - C23	0.2904	-0.8409	-0.4146	0.1022	-0.3124	0.2465	0.1552
N5 - N6	0.3105	-0.4837	-0.4729	0.1760	-0.2969	0.3722	0.1404
N4 - C17	0.2850	-0.5095	-0.4558	0.1642	-0.2916	0.3603	0.1032
F1 - C27	0.2346	-0.1891	-0.4429	0.1978	-0.2451	0.4466	0.0912
O2 - C13	0.1982	-0.1125	-0.2744	0.1232	-0.1513	0.4487	0.0423
O3 - C17	0.3514	-0.5005	-0.7559	0.3154	-0.4405	0.4172	0.0346
N4 - C24	0.2215	-0.2643	-0.3027	0.1183	-0.1844	0.3909	0.0202
N9 - C30	0.4531	-0.6139	-1.4028	0.6246	-0.7781	0.4453	0.0179

In this case, LTB contained 56 BCPs, with only a few of them included in table 1. From this table the positive $\nabla^2\rho(r)$ with respective $\rho(r)$ values indicates that the four intramolecular hydrogen bonds (closed-shell interactions) are presented at O3-H41, O3-H33, N4-H34, and C15-H32 and other the negative $\nabla^2\rho(r)$ values of BCPs are distinguished by shared covalent bond interactions. The local ED $H(r)$ is the sum of electronic kinetic ED $G(r)$ and electronic potential ED $V(r)$; this value of $H(r)$ and the $\nabla^2\rho(r)$ are used to define whether the hydrogen bond interactions are strong (or) weak if the $\nabla^2\rho\,(r) > 0$ & $H(r) > 0$, then the H-bonds are weak; if $\nabla^2\rho\,(r) < 0$ & $H(r) < 0$, the bonds are strong.[27]

Since, all four bonds are weakly coupled hydrogen bond interaction types in this instance, and the maximum interaction energy ($\Delta E_{HB} = -6.2498$ kcal/mol) of hydrogen bond was calculated ($\Delta E_{HB} = V(r)/2$) for O3-H41. Additionally, the ratio between $G(r)$ and $V(r)$ reveals that the BCPs are covalent or non-covalent, if $-(G/V)$ is greater than one,[28] the bonds are non-covalent otherwise they are covalent. The bond ellipticity $\mathcal{E}$, describes anisotropy of ED curvature and greatest ellipticity was found at BCP C15-H32.[29,30]

3.3. LOL and ELF

LOL and ELF studies were used to better understand the bond dynamics of the primary active sites. Schmider and Becke introduced LOL as a function of locating high localization regions. In terms of kinetic energy density, ELF and LOL have similar interpretations. In the present study, the color red signifies a region with a high ELF and LOL value, whereas the color blue shows a location with a low ELF and LOL value shown in figure 5. The electron localization and delocalization are also defined by the colors red and blue respectively.[31] As illustrated in figure 5, in the current study, the red region (electron depicted) around the hydrogen atoms of H42, H48, H47, etc., while blue zones (electron depletion) can be seen at N9, C30, C26, N8, C20, C14, C15, N4, etc., of the title compound. Also, the specific dark blue rings around a few nuclei of N9, C30, C15, N4, C26, and N8 in LTB demonstrate

those nuclei are maximum delocalized; the corresponding chemical environments N8=C26-N7, C18=C30≡N9, and C15=C14-C13 are found to be highest delocalization regions, they are visually exhibited with an electronic environment in figure 6.[32,33]

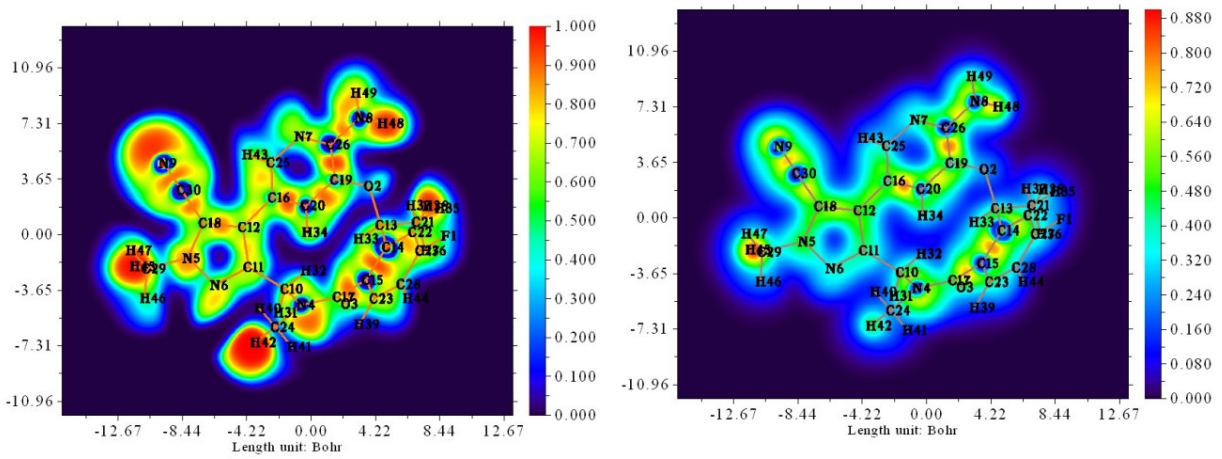

(a) (b)

Figure 5: (a) Electron localization function (ELF) map of static points on the main path, (b) Localized orbital locator (LOL) map of static points on the main path

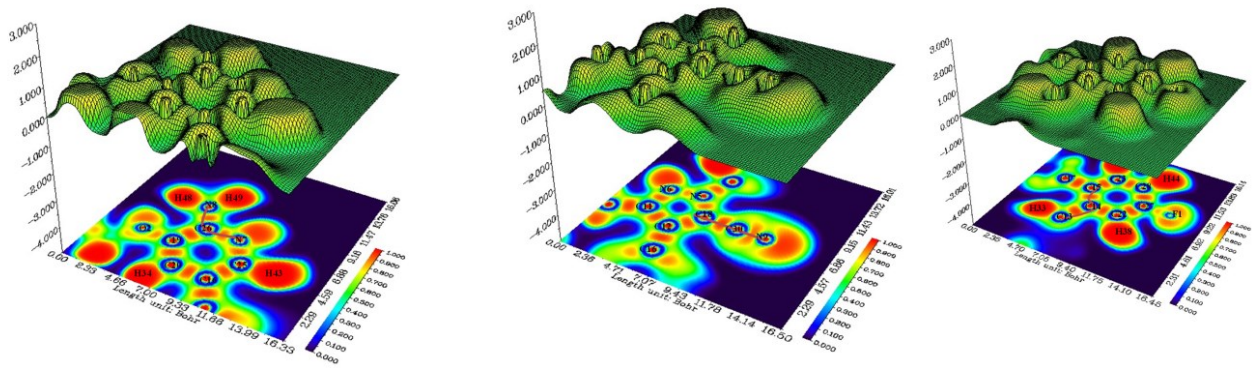

(a) (b) (c)

Figure 6: The ELF map with an electronic environment for the highest delocalization regions (a) N8=C26-N7, (b) C18=C30≡N9, and (c) C15=C14-C13

3.4. RDG analysis

RDG graph is used to identify the closed-shell weak interactions between atoms in a molecule, such as non-covalent interactions of inter and intramolecular hydrogen bonds, van der Waals connections (vdW), and so on. These non-bonded weak interactions in a very short range are represented by the NCI-Reduced density gradient (NCI-RDG) graph and it was plotted RDG versus sign $(\lambda_2)\rho$. These RDG energy values for the scatter plot can be estimated using the equation below,

$$\mathrm{RDG(r)} = \frac{1}{2(3\pi^2)^{1/3}} \frac{|\nabla \rho(r)|}{\rho\,(r)^{4/3}}$$

where $\rho(r)$ is the electron density, The repulsive steric effect, vdW interaction, and attractive hydrogen bond interaction are indicated in RDG map by the sign $(\lambda_2)\rho$ value greater than zero ($(\lambda_2)\rho > 0$), nearly zero ($(\lambda_2)\rho \approx 0$) and less than zero ($(\lambda_2)\rho < 0$) respectively and their corresponding colors of red, green, and blue were also used to identify them.[34,35] In the present study, from Fig.7, the sign $(\lambda_2)\rho$ region of red color (0.01 to 0.023a.u.) denotes a strong steric repulsive effect; the green color regions (-0.01 to -0.018a.u) reveals Van der walls interactions; and the dark green with the blue mixed spike (at nearly -0.02a.u.) exhibited the four intramolecular Hydrogen bonds (O3⋯H41, O3⋯H33, N4⋯H34, & C15⋯H32) were located in LTB.

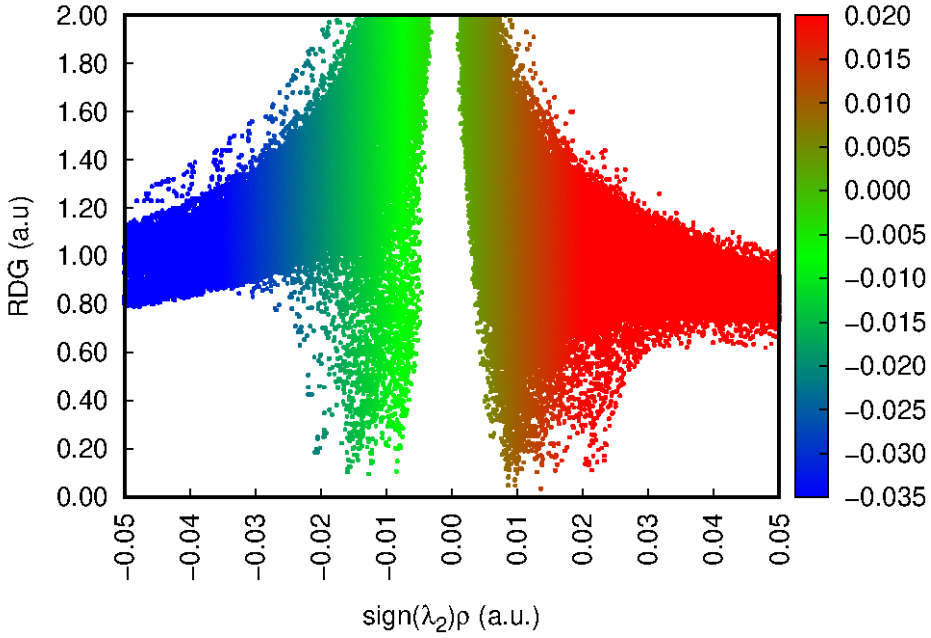

Figure 7: RDG Plots versus the electron density ρ multiplied by the sign of λ2 for LTB

3.5. Molecular Dynamics

In our study, Human DNA Topoisomerase I (70 Kda) complex with the Indenoisoquinoline MJ-II-38 and Covalent Complex with A 22 Base Pair DNA Duplex (1SC7),[36] APO and complexes with selected ligands from docking DRG were subjected to MD simulation of 100 ns. Following the stability of complex structures (potential energy), we must examine their stability under equilibrium (NVT and NPT) conditions (figure 8a). With a time, trajectory ranging from 0ps to 100ns, we calculated the temperature of the complex system. The temperature of protein, its bare state and all complex structures containing protein achieved a temperature value (300 K) within 100ps (table 2, figure 8b).

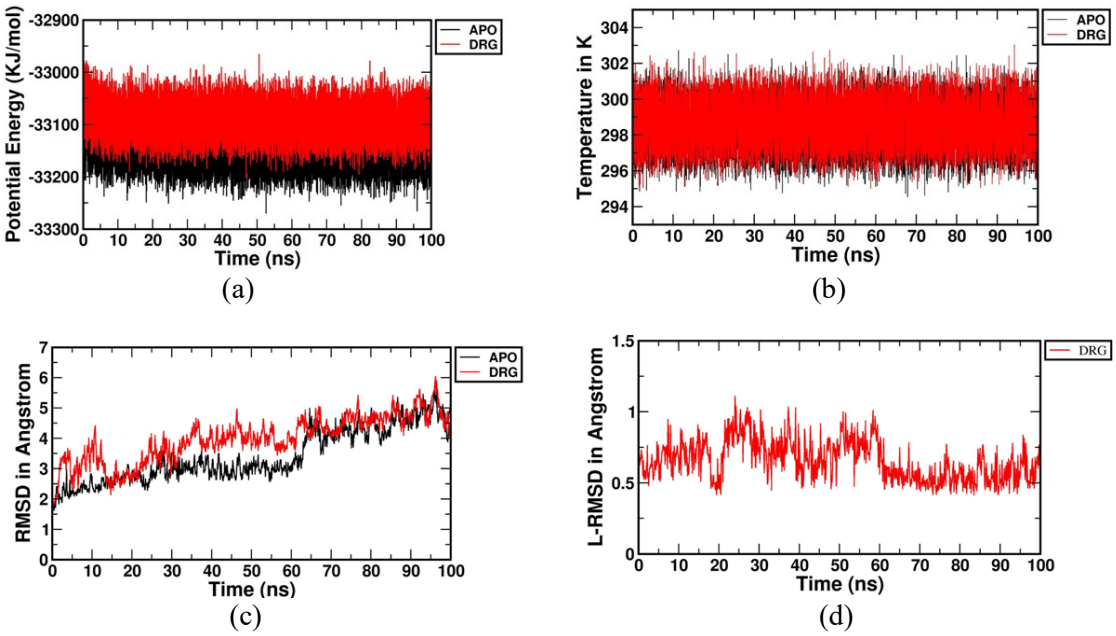

Figure 8: (a) Potential energy of APO and its complex with LTB, (b) Temperature of APO and its complex with complex, (c) RMSD of backbone atoms of APO and its complex with LTB complex, (d) Ligand Root means square deviation of backbone atoms of LTB complex

Table 2: Simulation quality table

Details	APO System		DRG System	
Total Energy (kcal/mol)	-273664.734	215.205	-273099.532	210.365
Potential energy (kcal/mol)	-331472.679	173.489	-330898.323	168.191
Temperature (K)	298.464	0.511	298.723	0.506
Pressure (bar)	1.427	33.737	1.131	33.274
Volume (Å³)	949189.654	614.732	947619.319	618.623

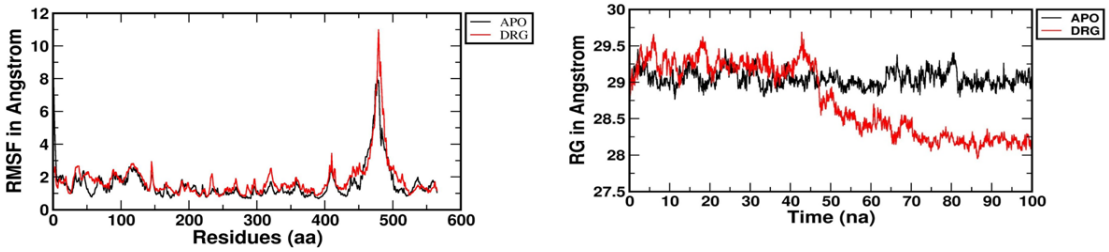

(a) (b)

Figure 9: (a) Root means square fluctuation of c-alpha atoms of APO and its complex with LTB (b) Rg of backbone atoms of APO and its complex with LTB

RMSD is an essential parameter for the determination of the differences between the two confirmations. The RMSD of 20 to 100ns results for APO and its complex with DRG are depicted in figure 8c.[37] During the 100ns simulation, it was observed that the APO and complexes are equilibrated after 20ns of time. The RMSD average is from 20 to 100 ns for APO and DRG complex proteins were 3.5 Å and 3.6 Å. The relative stability of apo and DRG complex throughout the simulation is represented by these RMSD data. The complexes also remained steady throughout the simulation. RMSF plots give the amino acids involved in bringing the overall structural deviation. The Liagnd RMSD values are calculated against the simulation timescale of 0 to 100ns. To understand the stability of the ligand with the protein, the RMSD of the ligand is required and it's average value from 0 to 100 ns were 0.07 Å (figure 8d).[38] The RMSF values and Rg average from 0 to 100 ns for APO and DRG complexes are 29.5 Å and 2.85 Å (figure 9a and b).[39,40]

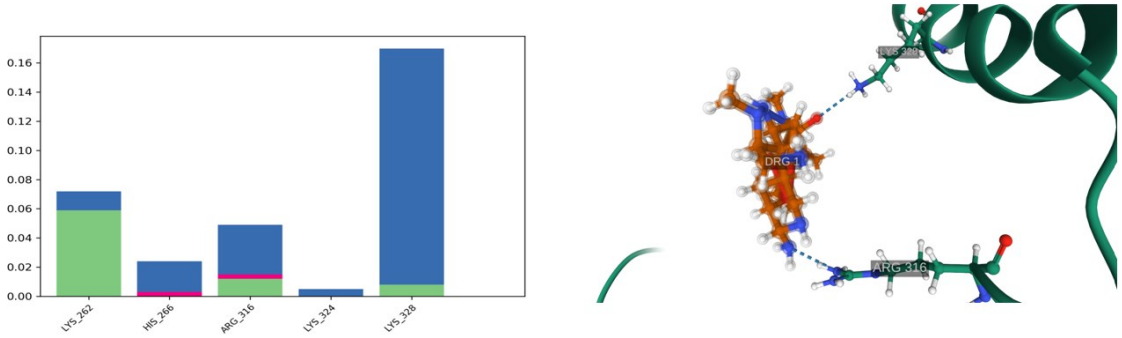

(a) (b)

Figure 10: (a) The H-Bond result of the complex with LTB, (b) multiple contacts between the interacting residues and LTB

The H-Bond result of the complex with LIG depicted in Fig.10a. LYS262, ARG316 which involves the ligand integrated with H-bond interaction, are examples of hydrogen bond based interactions. Water based interactions are also shown by HIS266 and LYS328, which entail the ligand interaction with a water bridge. Multiple contacts between the interacting residues and the ligand are seen in Fig.10b, with H-bond and water bridges accounting for the majority of contacts. An effective protein ligand assembly substantially promotes the creation of a stable complex by combining all of the

interactions in the active site. A successful protein-ligand assembly predicts a stable complex formation, given all of the interactions in the active site. To further validate our findings, experimental research will be required.

4. CONCLUSION

The wavefunction dependent reactivity properties and MD simulations are reported for the title compound. The red and yellow patches were caused by oxygen atoms, nitrogen atom in C≡N and pyridine ring in LTB and electronegative and electropositive patches were found over these atoms indicating nucleophilic and electrophilic attack sites. The bond ellipticity, describes anisotropy of ED curvature and greatest ellipticity was found at BCP C15-H32. Chemical environments N8=C26-N7, C18=C30≡N9, and C15=C14-C13 are found to be highest delocalization regions. The average Rg for APO and DRG complexes were 29.5 Å and 2.85 Å. MD simulations show that an effective protein ligand assembly promotes stable complex due to the interactions in the active site.

Acknowledgments. *The authors express their gratitude to Princess Nourah Bint Abdulrahman University Researchers Supporting Project number (PNURSP2022R13), Princess Nourah Bint Abdulrahman University, Riyadh, Saudi Arabia.*

Conflict of interest. *Authors declare no conflicts of interest.*

REFERENCES

1. L. A. Torre, F. Bray, R. L. Siegel, J. Ferlay, J. Lortet-Tieulent, A. Jemal. Global cancer statistics, 2012, *CA Cancer J. Clin*., **2015**, *65*, 87-108. https://doi.org/10.3322/caac.21262.
2. M. Reck, S. Popat, N. Reinmuth, D. De Ruysscher, K. M. Kerr, S. Peters. Metastatic non-small-cell lung cancer (NSCLC): ESMO clinical practice guidelines for diagnosis, treatment and follow-up, *Ann. Oncol*., **2014**, *25*, 27-39. https://doi.org/10.1093/annonc/mdu199.
3. S. Sarkar, G. Horn, K. Moulton, A. Oza, S. Byler, S. Kokolus, M. Longacre. Cancer development, progression and therapy: an epigenetic overview, *Int. J. Mol. Sci*., **2013**, *14*, 21087-21113. https://doi.org/10.3390/ijms141021087.
4. C. C. Cortez, P. A. Jones. Chromatin, cancer and drug therapies, Mutat. Res., **2008**, 647, 44-51. https://doi.org/10.1016/j.mrfmmm.2008.07.006.
5. A. Stoffel. Targeted therapies for solid tumors, *BioDrugs*, **2010**, *24*, 303-316. https://doi.org/10.2165/11535880-000000000-00000.
6. D. E. Gerber. Targeted therapies: A new generation of cancer treatments, *Am. Fam. Physician*, **2008**, *77*, 311-319. PMID: 18297955.
7. A. Pluzanski, A. Piorek, M. Krzakowski. Crizotinib in the treatment of non-small-cell lung carcinoma, *Contemp. Oncol. (Pozn),* **2012**, *16*, 480-484. https://doi.org/10.5114/wo.2012.32477.
8. N. James, V. Shanthi, K. Ramachandran. Density functional theory and molecular simulation studies of prioritizing anaplastic lymphoma kinase inhibitors, *Applied Biochemistry and Biotechnology*, **2020**, *190*, 1127-1146. https://doi.org/10.1007/s12010-019-03156-1.
9. J. Wu, J. Savooji, D. Liu. Second and third generation ALK inhibitors for non-small lung cancer, *J. Hematol. Oncol*., **2016**, *9*, 19. https://doi.org/10.1186/s13045-016-0251-8.
10. B. Preethi, V. Shanthi, K. Ramachandran. Investigation of nalidixic acid resistance mechanism in salmonella enteric using molecular simulation techniques, *Applied Biochemistry and Biotechnology*, **2015**, *177*, 528-540. https://doi.org/10.1007/s12010-015-1760-6.
11. V. Karthik, V. Shanthi, R. Rajasekaran, K. Ramachandran. Exploring the cause of oseltamivir resistance against H274Y neuraminidase by molecular simulation approach, *Appl. Biochem. Biotechnol*., **2012**, *167*, 237-249. https://doi.org/10.1007/s12010-012-9687-7.
12. A. T. Shaw, E. Felip, T. M. Bauer, B. Besse, A. Navarro, S. Postel-Vinay, J. F. Gainor, M. Johnson, J. Dietrich, L. P. James, J. S. Clancy, J. Chen, J. -F. Martini, A. Abbattista, B. J. Solomon. Lorlatinib in non-small-cell lung cancer with ALK or ROS1 rearrangement: an international, multicentre, open-label, single-arm first-in-man phase 1 trial, *Lancet Oncol.,* **2017**, *18*, 1590-1599. https://doi.org/10.1016/S1470-2045(17)30680-0.
13. M. J. Hochmair, H. Fabikan, O. Illini, C. Weinlinger, U. Setinek, D. Krenbek, H. Prosch, M. Rauter, M. Schumacher, E. Woll, R. Wass, E. Brehm, G. Absenger, T. Bundalo, P. Errhalt, M. Urban, A. Valipour. Later line treatment with lorlatinib in ALK- and ROS1 rearrangement-positive NSCLC: A retrospective, multicenter analysis, *Pharmaceuticals*, **2020**, *13*, 371. https://doi.org/10.3390/ph13110371.
14. S. Jiang, Y. Jin, R. Yan, Z. Wang. Detailed structural study of cyclic anticancer drug lorlatinib: spectroscopic and stereostructure investigation (IR, ECD and NMR) using density functional theory approach, *J. Mol. Struct*., **2021**, *1225*, 129295. https://doi.org/10.1016/j.molstruc.2020.129295.
15. N. Al-Zaqri, T. Pooventhiran, F. A. Alharthi, U. Bhattacharyya, R. Thomas. Structural investigations,

quantum mechanical studies on proton and metal affinity and biological activity predictions of selpercatinib, *J. Mol. Liquid*., **2021**, *325*, 114765. https://doi.org/10.1016/j.molliq.2020.114765.

16. N. Piergies, C. Paluszkiewicz, W. M. Kwiatek. Vibrational fingerprint of erlotinib: FTIR, RS and DFT studies, *Journal of Spectroscopy*, **2019**, 9191328. https://doi.org/10.1155/2019/9191328.
17. Gaussian 16, Revision A.03, M. J. Frisch, G. W. Trucks, H. B. Schlegel, G. E. Scuseria, M. A. Robb, J. R. Cheeseman, G. Scalmani, V. Barone, G. A. Petersson, H. Nakatsuji, X. Li, M. Caricato, A. V. Marenich, J. Bloino, B. G. Janesko, R. Gomperts, B. Mennucci, H. P. Hratchian, J. V. Ortiz, A. F. Izmaylov, J. L. Sonnenberg, D. Williams-Young, F. Ding, F. Lipparini, F. Egidi, J. Goings, B. Peng, A. Petrone, T. Henderson, D. Ranasinghe, V. G. Zakrzewski, J. Gao, N. Rega, G. Zheng, W. Liang, M. Hada, M. Ehara, K. Toyota, R. Fukuda, J. Hasegawa, M. Ishida, T. Nakajima, Y. Honda, O. Kitao, H. Nakai, T. Vreven, K. Throssell, J. A. Montgomery, Jr., J. E. Peralta, F. Ogliaro, M. J. Bearpark, J. J. Heyd, E. N. Brothers, K. N. Kudin, V. N. Staroverov, T. A. Keith, R. Kobayashi, J. Normand, K. Raghavachari, A. P. Rendell, J. C. Burant, S. S. Iyengar, J. Tomasi, M. Cossi, J. M. Millam, M. Klene, C. Adamo, R. Cammi, J. W. Ochterski, R. L. Martin, K. Morokuma, O. Farkas, J. B. Foresman, D. J. Fox, Gaussian, Inc., Wallingford CT, **2016**.
18. GaussView, Version 6.1, R. Dennington, T. A. Keith, J. M. Millam, Semichem Inc., Shawnee Mission, KS, **2016**.
19. E. R. Johnson, S. Keinan, P. Mori-Sanchez, J. Contreras-Garcia, A. J. Cohen, W. Yang. Revealing noncovalent interactions, *J. Am. Chem. Soc*., **2010**, *132*, 6498-6506. https://doi.org/10.1021/ja100936w.
20. AIMAll (Version 19.10.12), T. A. Keith, T. K. Gristmill Software, Overland Park KS, USA, **2019**.
21. K. J. Bowers, E. Chow, H. Xu, R. O. Dror, M. P. Eastwood, B. A. Gregersen, J. L. Klepeis, I. Kolossvary, M. A. Moraes, F. D. Sacerdoti, J. K. Salman, Y. Shan, D. E. Shaw. Scalable Algorithms for molecular dynamics simulations on commodity clusters, Proceedings of the ACM/IEEE Conference on Supercomputing (SC06), Tampa, Florida, **2006**.
22. R. I. Al-Wabli, K. S. Resmi, Y. S. Mary, C. Y. Panicker, M. I. Attia, A. A. El-Emam, C. Van Alsenoy. Vibrational spectroscopic studies, Fukui functions, HOMO-LUMO, NLO, NBO analysis and molecular docking study of (E)-1-(1,3-benzodioxol-5-yl)-4,4-dimethylpent-1-en-3-one, a potential precursor to bioactive agents, *J. Mol. Struct.,* **2016**, *1123*, 375-383. https://doi.org/10.1016/j.molstruc.2016.07.044.
23. Y. S. Mary, Y. S. Mary, K. S. Resmi, R. Thomas. DFT and molecular docking investigations of oxicam derivatives, *Heliyon*, **2019**, *5*, e02175. https://doi.org/10.1016/j.heliyon.2019.e02175.
24. V. V. Aswathy, S. Alper-Hayta, G. Yalcin, Y. S. Mary, C. Y. Panicker, P. J. Jojo, F. Kaynak-Onurdag, S. Armakovic, S. J. Armakovic, I. Yildiz, C. Van Alsenoy. Modification of benzoxazole derivative by bromine-spectroscopic, antibacterial and reactivity study using experimental and theoretical procedures, *J. Mol. Struct.,* **2017**, *1141*, 495-511. https://doi.org/10.1016/j.molstruc.2017.04.010.
25. E. D. Glendening, A. E. Reed, J. E. Carpenter, F. Weinhold. NBO Version 3.1, TCI, University of Wisconsin, Madison, **1998**.
26. V. S. Kumar, Y. S. Mary, K. Pradhan, D. Brahman, Y. S. Mary, G. Serdaroglu, A. S. Rad, M. S. Roxy. Conformational analysis and quantum descriptors of two new imidazole derivatives by experimental, DFT, AIM, molecular docking studies and adsorption activity on graphene, *Heliyon*, **2020**, *6*, e05182. https://doi.org/10.1016/j.heliyon.2020.e05182.
27. V. S. Kumar, Y. S. Mary, Y. S. Mary, G. Serdaroglu, A. S. Rad, M. S. Roxy, P. S. Manjula, B. K. Sarojini. Conformational analysis and DFT investigations of two triazole derivatives and its halogenated substitution by using spectroscopy, AIM and molecular docking, *Chemical Data Collections*, **2021**, *31*, 100625. https://doi.org/10.1016/j.cdc.2020.100625.
28. Y. S. Mary, Y. S. Mary, A. S. Rad, R. Yadav, I. Celik, S. Sarala. Theoretical investigation on the reactive and interaction properties of sorafenib-DFT, AIM, spectroscopic and Hirshfeld analysis, docking and dynamics simulation, *Journal of Molecular Liquids*, **2021**, *330*, 115652. https://doi.org/10.1016/j.molliq.2021.115652.
29. S. G. Neogi, A. Das, P. Chaudhury. Investigation of plausible mechanistic pathways in hydrogenation of η^5-$(C_5H_5)_2Ta(H)=CH_2$: an analysis using DFT and AIM techniques, *J. Mol. Model.,* **2014**, *20*, 2132. https://doi.org/10.1007/s00894-014-2132-9.
30. P. Srinivasan, S. N. Asthana, R. B. Pawar, P. Kumaradhas. A theoretical charge density study on nitrogen-rich 4,4’,5,5’-tetranitro-2,2’-bi-1*H*-imidazole (TNBI) energetic molecule, *Struct. Chem*., **2011**, *22*, 1213-1220. https://doi.org/10.1002/s11224-011-9815-y.
31. J. Zhou, L. Zhu, J. Chen, W. Wang, R. Zhang, Y. Li, Q. Zhang, W. Wang. Degradation mechanism of zearalenone ring-cleavate by zearalenone hydrlase RmZHD: A QM/MM study, *Science of the Total Environment*, **2020**, *709*, 135897. https://doi.org/10.1016/j.scitotenv.2019.135897.
32. J. S. Al-Otaibi, Y. S. Mary, Y. S. Mary, R. Yadav. Structural and reactivity studies of pravadoline-An ionic liquid, with reference to its wavefunction-relative properties using DFT and MD simulation*, J.*

Mol. Struct., **2021**, *1245*, 131074. https://doi.org/10.1016/j.molstruc.2021.131074.

33. Y. S. Mary, Y. S. Mary, K. S. Resmi, S. Sarala, R. Yadav, I. Celik. Modeling the structural and reactivity properties of hydrazono methyl-4*H*-chromen-4-one derivatives-wavefunction-dependent properties, molecular docking and dynamics simulation studies, *Journal of Molecular Modeling*, **2021**, *27*, 186. https://doi.org/10.1007/s00894-021-04800-6.
34. F. Alman, N. Issaoui, A. S. Kazachenko. Intermolecular hydrogen bond interactions in the thioura/water complexes (Thio-$(H_2O)_n$) (n=1, …, 5): X-ray, DFT, NBO, AIM and RDG analyses, *J. Mol. Model*., **2020**, *26*, 161. https://doi.org/10.1007/s00894-020-04423-3.
35. C. Chiter, A. Bouchama, T. N. Mouas, H. Allal, M. Yahiaoui, I. Warad, A. Zarrouk, A. Djedouani. Synthesis, crystal structure, spectroscopic and hirshfeld surface analysis, NCI-RDG, DFT computations and antibacterial activity of new asymmetrical azines, *J. Mol. Struct.,* **2020**, *1217*, 128376. https://doi.org/10.1016/j.molstruc.2020.128376.
36. B. L. Staker, M. D. Feese, M. Cushman, Y. Pommier, D. Zembower, L. Stewart, A. B. Burgin. Structures of three classes of anticancer agents bound to the human topoisomerase I-DNA covalent complex, *J. Med. Chem*., **2005**, *48*, 2336-2345. https://doi.org/10.1021/jm049146p.
37. Y. S. Mary, Y. S. Mary, S. Armakovic, S. J. Armakovic, R. Yadav, I. Celik, P. Mane, B. Chakraborty. Stability and reactivity study of bio-molecules brucine and colchicines towards electrophile and nucleophile attacks: Insight from DFT and MD simulations, *Journal of Molecular Liquids*, **2021**, *335*, 116192. https://doi.org/10.1016/j.molliq.2021.116192.
38. Y. S. Mary, Y. S. Mary, O. Temiz-Arpaci, R. Yadav, I. Celik. DFT, docking, MD simulation and vibrational spectra with SERS analysis of a benzoxazole derivative: an anti-cancerous drug, *Chemical Papers*, **2021**, *75*, 4269-4284. https://doi.org/10.1007/s11696-021-01659-y.
39. M. Smitha, Y. S. Mary, Y. S. Mary, G. Serdaroglu, P. Chowdhury, M. Rana, H. Umamahesvari, B. K. Sarojini, B. J. Mohan, R. Pavithran. Modeling the DFT structural and reactivity studies of a pyrimidine-6-carboxylate derivative with reference to its wavefunction-dependent, MD simulations and evaluation for potential antimicrobial activity, *J. Mol. Struct*., **2021**, *1237*, 130397. https://doi.org/10.1016/j.molstruc.2021.130397.
40. Y. S. Mary, Y. S. Mary, V. Chandramohan, N. Kumar, C. Van Alsenoy, M. C. Gamberini. DFT and MD simulations and molecular docking of co-crystals of octafluoro-1,4-diiodobutane with phenazine and acridine, *Struct. Chem*., **2020**, *31*, 2525-2531. https://doi.org/10.1007/s11224-020-01616-7.

Corresponding author: **Y. Sheena Mary**
Thushara, Neethinagar-64, Pattathanam, Kollam, Kerala, India
E-mail: marysheena2018@rediffmail.com.